PHYSICAL REVIEW B **92**, 014302 (2015)

X-ray absorption spectroscopy study of local dynamics and thermal expansion in ReO_3

J. Purans,[1,2] P. Fornasini,[1,*] S. E. Ali,[1] G. Dalba,[1] A. Kuzmin,[2] and F. Rocca[3]
[1]*Dipartimento di Fisica, Università di Trento, Via Sommarive 14, I-38123 Povo (Trento), Italy*
[2]*Institute of Solid State Physics, University of Latvia, Kengaraga Street 8, LV-1063 Riga, Latvia*
[3]*IFN-CNR, Istituto di Fotonica e Nanotecnologie del Consiglio Nazionale delle Ricerche, Unità "FBK-Photonics" di Trento,*
Via alla Cascata 56/C, I-38123 Povo (Trento), Italy

(Received 18 June 2008; revised manuscript received 8 June 2015; published 16 July 2015)

The thermal expansion of polycrystalline ReO_3 is studied in vacuum by x-ray diffraction from 300 to 600 K and by extended x-ray absorption fine structure (EXAFS) at the Re L_3 edge from 30 to 600 K. A detailed EXAFS analysis is presented up to the sixth coordination shell around Re. The crystal thermal expansion is weak throughout the explored range, negative below 100 K, positive from 150 to 500 K, and negative again above 500 K. The analysis of mean square relative displacements obtained by EXAFS and of mean square displacements available from x-ray and neutron diffraction measurements confirms the presence of significant static disorder in the investigated samples. EXAFS results suggest that below 500 K in ReO_3 at least some of the octahedra are slightly and disorderly rotated by an average angle $\langle\theta\rangle$, whose value decreases when the temperature increases. This explains why ReO_3, in spite of the possibility of supporting rigid unit modes, shows a weak positive expansion at increasing temperatures, from 150 up to 500 K. Results are discussed and compared with recent experimental and theoretical work on materials characterized by negative thermal expansion.

DOI: 10.1103/PhysRevB.92.014302 PACS number(s): 63.20.−e, 65.40.De, 61.05.cj

I. INTRODUCTION

The interest in negative thermal expansion (NTE) and related phenomena [1,2] has grown continuously since the discovery that in materials like AW_2O_8 (A = Zr, Hf) and $A(CN)_2$ (A = Zn, Ni) the strong contraction upon heating extends over a wide temperature range [3–6]. These compounds can be considered open framework structures made up of loosely connected, corner-linked, tetrahedral and octahedral units [7,8].

In parallel, the interest in ReO_3-type perovskites has recently been renewed by the discovery of large NTE in cubic ScF_3 over a wide temperature range [9], compared with the much less intense effect measured for ReO_3 [10,11]. The rhenium trioxide structure is often used to illustrate the interconnection between the rigid unit modes (RUMs) and the NTE. Low-frequency RUMs induce cooperative rotations of the polyhedra, leading to the large transverse motion of oxygen atoms linking adjacent polyhedra. These rotations are thought to be at the origin of the observed contraction of the unit cell.

Rhenium trioxide has a unique perovskite-type structure (ABO_3), with a simple-cubic Bravais lattice ($Pm\bar{3}m$ space group) composed of ReO_6 octahedra joined by the corners, the A sites being vacant (see Fig. 1). The presence of empty A sites permits large rotations of the ReO_6 octahedra. No evidence has been found of phase transitions at ambient pressure in the low-temperature range, up to 500 K [12]. The stability of the cubic lattice has been explained in terms of interaction between phonons and conduction electrons [13].

ReO_3 is sometimes referred to as a "covalent metal," since it has a high metallic conductivity related to the delocalization of the rhenium single *d* electron below 500 K while the Re-O bonding is strongly covalent [14–17].

On the other hand, ReO_3 exhibits a number of phase transitions under high pressure [18–20]. A buckling of the Re-O-Re linear chain, induced by pressure, is at the origin of the so-called "compressibility collapse" [21]: the transverse shift of the average oxygen positions corresponds to a rotation around the main cubic axes of the ReO_6 octahedra.

Large transverse displacements of the bridging oxygen atoms in ReO_3 have been measured since the early diffraction [18,22] and extended x-ray absorption fine structure (EXAFS) [23] experiments also at ambient pressure, i.e., for samples considered undistorted. The possibility of statically disordered octahedral rotations at ambient pressure was originally suggested by Yacoby *et al.* [24]. In a successive EXAFS study by Houser and Ingalls [23], the use of an *ab initio* multiple-scattering approach was used to follow the bending of Re-O-Re bonds as a function of pressure. It was found that the length of multiple-scattering EXAFS signals generated within the Re-O-Re chains measures the transverse displacements of the oxygen atom located between two adjacent rhenium atoms, as opposed to an average oxygen position, probed by diffraction. In particular, an effective Re-O-Re bridging angle of 172° was determined at ambient pressure: this value was attributed to thermal motion of the oxygen atom perpendicular to the linkage, not to a permanent tilt of the angle, as measured by both x-ray diffraction (XRD) and EXAFS at higher pressure [23]. This result has been substantially confirmed by recent simulations of the Re L_3-edge EXAFS spectra using classical molecular dynamics [25] and reverse Monte Carlo [26] methods, which predict that the bond angle distribution function for the Re-O-Re bridging angle peaks in the range $\simeq$175–172°, depending on the temperature.

Note that all previous EXAFS studies [23,25–30] considered the average structure of ReO_3 to be cubic ($Pm\bar{3}m$), in full agreement with diffraction data [11,18,22,31–33] as well as with a recent analysis based on the atomic pair distribution function of high-resolution neutron time-of-flight

---

[*] paolo.fornasini@unitn.it

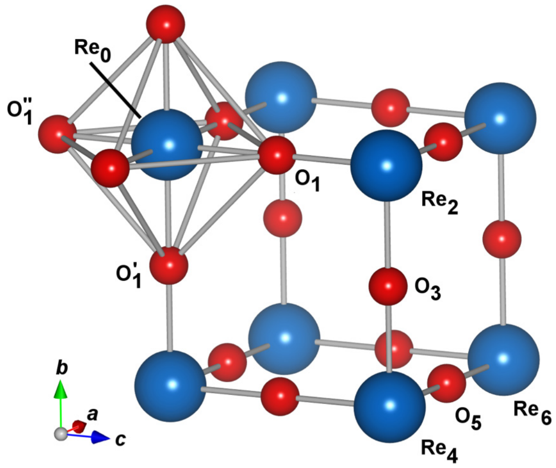

FIG. 1. (Color online) Fragment of the perovskite-like ReO_3 crystallographic structure [18] composed of ReO_6 regular octahedra joined by corners. Atoms in the first six coordination shells (O_1, Re_2, O_3, Re_4, O_5, Re_6) around rhenium atom Re_0 are labeled. The additional two oxygen atoms (O_1', O_1''), involved in the calculation of multiple-scattering signals, are also indicated.

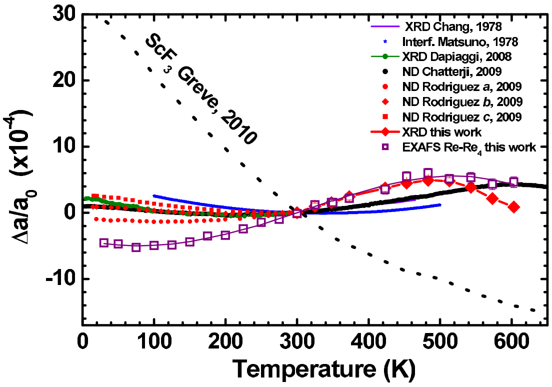

FIG. 2. (Color online) Temperature dependence of the variation of the ReO_3 lattice parameter $\Delta a(T)/a_0$, measured by ESXD at and above 300 K [present work; filled (red) diamonds] and calculated from the first EXAFS cumulant of the Re_4 coordination shell according to the procedure described in the text [open (purple) squares]. Also shown are the following results: (i) XRD, from Chang and Trucano [12] (violet line) and from Dapiaggi and Fitch [11] (filled green circles); (ii) neutron diffraction, from Chatterij *et al.* [32] (filled black circles) and Rodriguez *et al.* [33] (different powdered samples according to Ref. [33]: ReO_3-a, filled red circles, ReO_3-b, filled (red) diamonds; and ReO_3-c, filled (red) squares); (iii) laser interferometry, from Matsuno *et al.* [35] [(blue) stars]; and (iv) diffraction on ScF_3, from Ref. [9] (dashed black line).

total scattering data [34]. However, these findings do not exclude the presence of randomly distributed local distortions as suggested originally by Yacoby [24] and more recently by Rodriguez [33].

Because of its framework structure, where the application of the RUM model is expected to produce NTE over a wide temperature range, many efforts have been devoted to quantifying the thermal expansion of ReO_3 in the past. Even though the available data show considerably different behaviors, they all agree in measuring a very small change in the lattice parameter with temperature. In Fig. 2 we compare the results of the most important thermal expansion experiments on ReO_3, together with a very recent result obtained for ScF_3, a crystal having the same cubic phase as ReO_3: the difference between the two isostructural crystals is quite large [9].

Until recently, the thermal expansion data for cubic ReO_3 were available from the interference [35] and XRD [12,21,36,37] measurements, showing surprisingly different trends with temperature: in Ref. [35] an NTE coefficient was measured on a single crystal at low temperatures: it was -2×10^{-6} K^{-1} below 100 K, then it increased rather rapidly with temperature and became positive above 340 K, up to 500 K; on the contrary, an average positive expansion coefficient was quoted in Refs. [12] and [36] from 100 to 500 K. Later, a weak positive thermal expansion was found in Refs. [21] and [37]. In our preliminary report on combined XRD and absorption studies, we measured NTE only below 100 K [10].

For comparison of ReO_3 with isostructural cubic systems, we remember that the thermal expansion coefficient of WO_3 is $\alpha \simeq 3.9 \times 10^{-6}$ K^{-1} between 300 and 500 K [38], while that of cubic ScF_3, [9] is negative: $\alpha \simeq -14 \times 10^{-6}$ K^{-1} between 30 and 1100 K.

Over the last years, neutron and synchrotron radiation techniques (diffraction and EXAFS) available at large-scale facilities have been applied to high-accuracy studies of thermal expansion on powdered ReO_3 samples. By neutron [31,32] and XRD [11] measurements, NTE has been observed up to 200 K. The most recent neutron-diffraction studies [33] were performed on three samples up to 300 K: they document different intensities and trends for the thermal expansion coefficients. The authors conclude that the transition temperature from negative to positive thermal expansion is significantly dependent on the sample production and manipulation history.

Only a few measurements have extended the temperature range up to 600 K: we were the first who measured a very weak but positive trend up to 500 K and a reverse negative behavior up to decomposition temperature [10]. The most recent neutron-diffraction studies confirm the same trend: thermal expansion is weak throughout the explored range, negative at low temperatures, positive from 200 to 600 K, and negative again above 600 up to 680 K [32].

The weakness, or absence, of NTE is at odds with the vibrations of oxygen atoms perpendicular to the Re-O-Re linkage and with the recent results of ScF_3 having the expected NTE over a wide temperature range. The main goal of the present work is to contribute to the solution of this controversial issue with a detailed analysis of temperature-dependent XRD and EXAFS measurements performed contemporaneously. The basic idea is to exploit the complementarity of the two techniques in order to get information on the anisotropy of the local dynamical behavior and on the thermal expansion of selected interatomic bonds.

For crystals with atoms only in special positions, like undistorted perovskites, the distance $R = |\langle \mathbf{r}_b \rangle - \langle \mathbf{r}_a \rangle|$ between the average positions of any two atoms can be obtained from the cell parameters measured in diffraction experiments, and its temperature variation ΔR is proportional to the macroscopic thermal expansion. EXAFS experiments measure the average value of the instantaneous distances, $\langle r \rangle = \langle |\mathbf{r}_b - \mathbf{r}_a| \rangle$. The distances R and $\langle r \rangle$, and the corresponding thermal expansions, are different, owing to thermal vibrations perpendicular to the direction of the interatomic bond [39,40].

The *absolute* thermal ellipsoids measured for every atom by diffraction experiments can be parameterized, in the case of axial symmetry around the bond direction, in terms of two mean square displacements (MSDs), one parallel and one perpendicular to the bond. EXAFS is sensitive to the *relative* displacements of the pair of absorber and backscatter atoms [41]. The parallel mean square relative displacement (MSRD) $\langle \Delta u_{\|}^2 \rangle$ can be directly measured from EXAFS experiments. The perpendicular MSRD $\langle \Delta u_{\perp}^2 \rangle$ can be obtained from the knowledge of both interatomic distances measured by EXAFS and diffraction, $\langle r \rangle$ and R, respectively [42,43].

Temperature-dependent measurements on several different systems—like Ge, Ag_2O, Cu_2O, and CuCl—have shown that, by considering bond distances in addition to MSRDs, it is possible to enhance the potential of EXAFS to probe the local dynamical origin of NTE in crystals [39,40,44,45]. The availability of original experimental setups at the European Synchrotron Radiation Facility [46,47], designed to measure contemporarily both EXAFS and XRD, enhances the effectiveness of NTE studies [48].

To our knowledge, no temperature-dependent EXAFS studies have been performed on ReO_3 until now, except for our two previous works [29,30], done at atmospheric pressure in air, where the attention was focused on the parallel MSRDs of those coordination shells that can be treated within a single-scattering formalism. In this work we present the analysis of high-quality EXAFS data over a wide temperature range, which takes into account multiple-scattering effects, thus allowing us to access the structural information from the second and third coordination shells around rhenium atoms. This information, together with that obtained by complementary XRD technique, allows us to accurately monitor the thermal expansion of ReO_3 over a wide range of temperatures from 30 to 600 K.

The paper is organized as follows. In Sec. II, the relevant details of the sample preparation and XRD and EXAFS measurements are given. Section III is dedicated to the procedures of data analysis and to a critical comparison between the *ab initio* and the semiempirical modeling. The results obtained are presented in Sec. IV. Sections V and VI are dedicated to discussion and conclusions, respectively.

II. EXPERIMENTAL PROCEDURES

A commercial ReO_3 powder (from Metalli Preziosi S.p.A.), 99.9% pure, was finely ground and homogeneously deposited on a polytetrafluoroethylene membrane by a sonication technique. The thickness of the sample was optimized so as to obtain a jump $\Delta(\mu x) \simeq 1$ at the Re L_3 absorption edge. The sample was divided into two parts, A and B, to be used in low- and high-temperature measurements, respectively (see below).

Both XAFS and XRD measurements were performed at the BM29 beam line [46,47] of the European Synchrotron Radiation Facility in Grenoble. Storage ring energy and average current were 6.0 GeV and 200 mA, respectively.

The XAFS spectra at the Re L_3 edge were measured in the energy range from 10 200 to 11 940 eV in transmission mode. A Si(111) double-crystal monochromator was used, and harmonic rejection was achieved by 30% detuning the two crystals from the parallel alignment. The spectra were recorded by two ionization chambers filled with argon gas. The pre-edge and edge regions were sampled at constant energy steps, $\Delta E = 5$ and 0.3 eV, respectively, whereas the EXAFS region was sampled at constant photoelectron wave-vector steps, $\Delta k = 0.025$ Å^{-1}. The overall energy resolution (FWHM) was 1.5 eV. The white-line edge positions were reproducible with a precision of better than 0.1 eV. At least two spectra were recorded at each temperature.

Low-temperature (from 30 to 350 K) XAFS measurements were done on sample A using a liquid helium closed-cycle cryostat with a heating resistor. The temperature was stabilized within ±2 K. For geometrical reasons, no XRD measurements could be done in this sample-holder configuration.

High-temperature (from 300 to 600 K) XAFS and XRD measurements were done on sample B, placed in a graphite cell mounted in a multipurpose vacuum oven [46]. The temperature was stabilized within 5 K. XRD measurements were done in energy scanning mode (ESXD) [47] using a set of four CdZnTe solid-state detectors placed at the fixed 2θ scattering angles 8.097°, 18.606°, 30.139°, and 46.871°. The scans were performed, using an acquisition time of 4 s per point and an energy step of 5 eV, in the six energy intervals 14.05–14.70, 14.90–15.10, 15.45–15.70, 22.70–23.10, 23.20–23.50, and 23.70–24.00 KeV. As a result, the Bragg-scattering from planes (100), (110), (210), (211), (222), (320), and (321) was recorded.

III. XAFS DATA ANALYSIS

X-ray absorption spectra were treated using the EDA software package [49]. Since an uncertainty of a few hundredths electron volt in energy leads to an uncertainty of a few tens of femtometers in distance differences, the edges of all spectra were carefully aligned to within 0.02 eV.

The XANES part of the spectra, shown in Fig. 3 at selected temperatures, is dominated by a prominent white line, located at about 10540 eV. Contrary to our previous study [30], where all experiments were performed in air, no change in the absorption edge position (within the monochromator uncertainty) or in the white-line intensity has been found in the present work, which was done in vacuum. This proves that no modification of the ReO_3 crystalline phase has occurred in our experiment up to the highest temperature (600 K), which is, at any rate, lower than the ReO_3 decomposition temperature (∼673 K) [50]. The EXAFS signals were extracted following a standard procedure. The photoelectron energy origin E_0 was set at the maximum of the first derivative of the absorption coefficient. The EXAFS signals $\chi(k)k^2$ and their Fourier transforms (FTs) are shown in Fig. 4 at selected temperatures. The peak positions in FTs are shifted with respect to crystallographic distances because FTs were calculated without phase-shift correction. A significant decrease in the peak amplitude when the temperature increases is well visible in Fig. 4. However, on the whole, the shape of

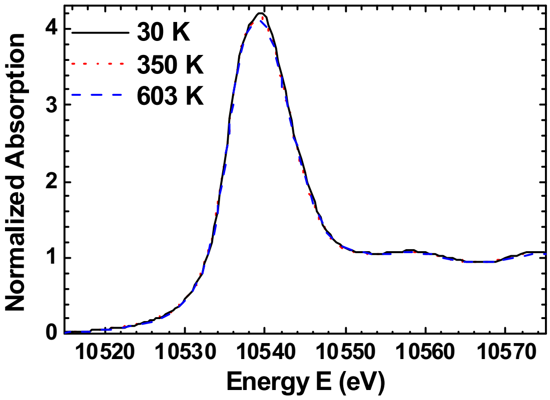

FIG. 3. (Color online) Temperature dependence of the experimental Re L_3-edge XANES spectra in ReO$_3$. The ”white line” at 10 540 eV corresponds to the dipole allowed transition $2p_{3/2}(\text{Re}) \rightarrow 5d(\text{Re}) + 2p(\text{O})$ [30].

both the EXAFS signals and their FTs remains similar up to the highest temperature ($T = 600$ K). The origin of the peaks in FTs was investigated in previous works [28,51]: they are due to the single- and multiple-scattering effects involving the first six coordination shells ($\text{O}_1, \text{Re}_2, \text{O}_3, \text{Re}_4, \text{O}_5, \text{Re}_6$) around the absorbing rhenium atom (Re$_0$).

The quantitative analysis of EXAFS spectra was based on two complementary methodologies: (a) *ab initio* modeling of the whole EXAFS signal and determination of the structural and dynamical parameters by nonlinear best fit to the experimental signal and (b) single-scattering analysis of the Fourier-filtered single-shell contributions, using the lowest temperature spectra as reference for scattering amplitudes, phase shifts, and inelastic terms (here referred to as the “semiempirical” approach).

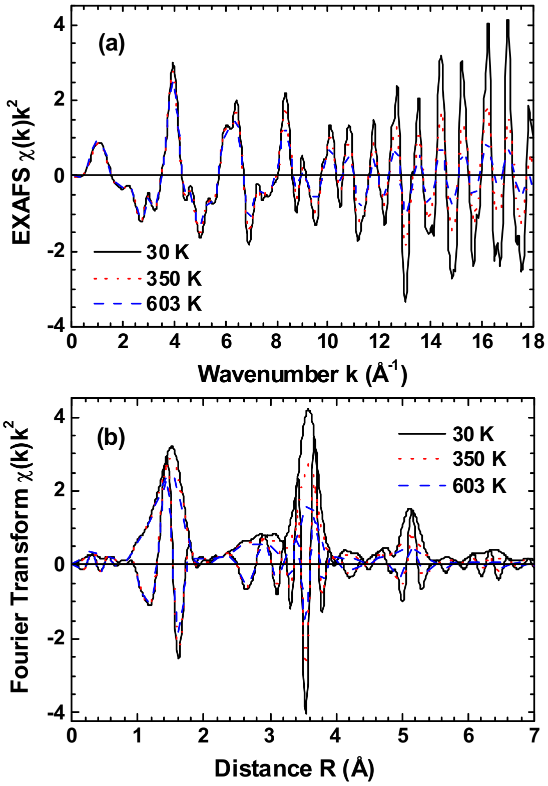

FIG. 4. (Color online) Temperature dependence of (a) the experimental Re L_3-edge EXAFS $\chi(k)k^2$ spectra and (b) their Fourier transforms. Both modulus and imaginary part are shown in (b).

A. *Ab initio* EXAFS modeling

The analysis based on the *ab initio* real-space multiple-scattering theory was done using the FEFF8 [52,53] and FEFFIT [54] codes. Calculations of the scattering amplitude and phase functions were performed, by the FEFF8 code, for a cluster representing part of a ReO$_3$ crystal with lattice parameter $a_0 = 3.75$ Å [18], centered on a rhenium atom and having a radius of 8 Å. The cluster potential, of the muffin-tin (mt) type with radii $R_{\text{mt}}(\text{Re}) = 1.223$ Å and $R_{\text{mt}}(\text{O}) = 0.932$ Å, was calculated in a self-consistent way. The complex Hedin-Lundqvist exchange-correlation potential [55,56] was used to account for inelastic effects. The list of paths used in the fit is given in Table I.

The fits to experimental spectra were performed in the back-transformed k space by the FEFFIT code. The R-space interval took into account the contributions from 0.5 to 5.7 Å, which correspond to the first five coordination shells around rhenium atoms. Three k-space intervals were used in the fits, 1–18, 2–18, and 4–18 Å^{-1}, respectively, to check the stability of the results and evaluate their error bars.

The possibility of simultaneously fitting the EXAFS signals obtained at different temperatures, implemented in the analysis codes, allowed us to analyze rather accurately the EXAFS signal from the peak at 3.5 Å in FTs (see Fig. 4), which is dominated by the second shell contribution but includes also the multiple scattering (MS) effects within the Re$_0$-O$_1$-Re$_2$ chains and a contribution from the third coordination shell. Note that a correct evaluation of the temperature dependence

TABLE I. Scattering paths (SS, single scattering; DS, double scattering; TS, triple scattering) calculated by the FEFF8 code [52,53] and used in the fit by the FEFFIT code [54]. Atoms in the path are labeled as in Fig. 1. Path lengths correspond to the lattice parameter $a_0 = 3.75$ Å.

Index	Path	Path type	Path degener.	Half–path length (Å)
1	Re$_0$-O$_1$-Re$_0$	SS	6	1.875
2	Re$_0$-O$_1$-O$'_1$-Re$_0$	DS	24	3.201
3	Re$_0$-Re$_2$-Re$_0$	SS	6	3.750
4	Re$_0$-O$_1$-O$''_1$-Re$_0$	DS	6	3.750
5	Re$_0$-O$_1$-Re$_2$-Re$_0$	DS	12	3.750
6	Re$_0$-O$_1$-Re$_0$-O$''_1$-Re$_0$	TS	6	3.750
7	Re$_0$-O$_1$-Re$_0$-O$_1$-Re$_0$	TS	6	3.750
8	Re$_0$-O$_1$-Re$_2$-O$_1$-Re$_0$	TS	6	3.750
9	Re$_0$-O$_1$-Re$_0$-O$'_1$-Re$_0$	TS	24	3.750
10	Re$_0$-O$_3$-Re$_0$	SS	24	4.193
11	Re$_0$-O$_1$-O$_3$-Re$_0$	DS	48	4.360
12	Re$_0$-O$_1$-O$'_1$-O$_1$-Re$_0$	TS	24	4.527
13	Re$_0$-O$_1$-O$_3$-O$_1$-Re$_0$	TS	24	4.527
14	Re$_0$-Re$_4$-Re$_0$	SS	12	5.303
15	Re$_0$-O$_5$-Re$_0$	SS	30	5.625

for these two coordination shells is crucial for understanding the lattice dynamics and thermal expansion in ReO_3.

Our starting model included several fitting parameters: [54] the ΔE_0 correction, the amplitude scaling factor S_0^2, the lattice correction parameter A_{expan}, a linear thermal expansion coefficient α_0, and a set of second cumulants $C_2^*(T)$. The parameters ΔE_0, S_0^2, and A_{expan} have no temperature dependence and, thus, have been fixed to the same value at all temperatures. The best-fitting final values were $\Delta E_0 = 5.1 \pm 0.5$ eV, $S_0^2 = 0.82 \pm 0.06$, and $A_{\text{expan}} = (3 \pm 1) \times 10^{-4}$.

A unique, very small linear thermal expansion coefficient was obtained from the fit, $\alpha_0 = (0.2 \pm 0.8) \times 10^{-6}$ K^{-1}. It was impossible, by the *ab initio* method, to distinguish the different coefficients for the different coordination shells, or the difference between EXAFS and XRD thermal expansion. Better results could be obtained with the semiempirical method, at least for the first and fourth shells (see below).

The most relevant results from the *ab initio* method concern the second cumulants (or MSRD) C_2^*, which were independently fitted at each temperature, in order to check if there is any deviation from the usual temperature dependence, described by the Einstein or Debye model [29]. At each temperature, we used the same values of second cumulants for several scattering paths corresponding to the same group of atoms: in particular, $C_{2,1}^* = C_{2,7}^*$, $C_{2,2}^* = C_{2,9}^* = C_{2,12}^*$, $C_{2,4}^* = C_{2,6}^*$, and $C_{2,11}^* = C_{2,13}^*$, where the second indices correspond to the path indices in Table I.

In the starting model, we considered different values of the second cumulants for paths 3, 5, and 8, corresponding to atoms located in the linear Re_0-O_1-Re_2 chain, which are responsible for the strongest MS contributions [28]. This model can take into account the effect of the oxygen motion perpendicular to the Re_0-O_1 bond, which could contribute in a slightly different way for the three paths and is expected to be large from XRD data [22]. However, we found that the three second cumulants converge during the fit procedure to close values at all temperatures, therefore we used only one fitting parameter, $C_{2,3}^* = C_{2,5}^* = C_{2,8}^*$, in the final model.

Typical examples of the best-fit results are shown in Fig. 5. The overall agreement between the experimental and the theoretical signals is very good. The residual discrepancy below 6 Å^{-1}, increasing when k decreases, is presumably due to inadequacy of theoretical simulations.

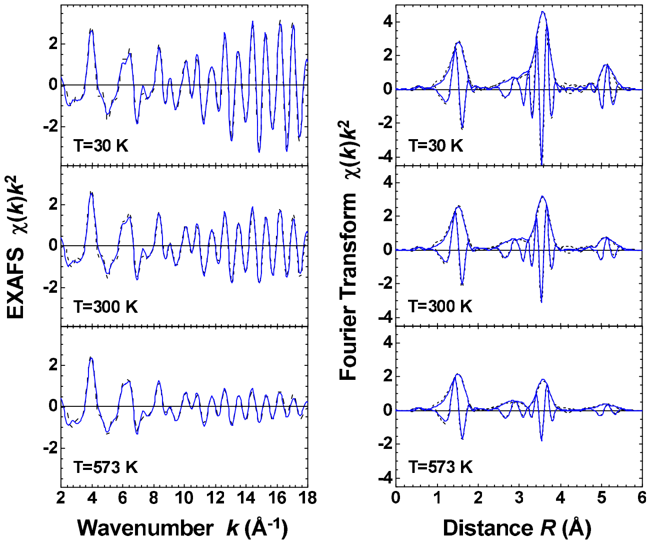

FIG. 5. (Color online) Best-fit results for the EXAFS $\chi(k)k^2$ signals (left) and the corresponding Fourier transforms (right) at three temperatures, obtained by the FEFFIT code. Dashed line, experiment; solid line, calculation. The fit was performed in the k-space interval 2–18 Å^{-1}.

B. Single-shell EXAFS analysis

For every scattering path, the EXAFS signal is expressed as the average over a one-dimensional distribution of distances [57,58], which, for moderately disordered systems, can be parameterized in terms of its leading cumulants C_i^* [59,60]. The first cumulant $C_1^* = \langle r \rangle$ is the average value of the distribution $\rho(r)$. The second cumulant (EXAFS Debye-Waller exponent) is the variance of the distribution and corresponds, to a good approximation, to the parallel MSRD, $C_2^* = \langle \Delta u_{\|}^2 \rangle$. The third cumulant measures the asymmetry of the distribution.

In the semiempirical approach [59,60], the experimental amplitude and phase-shift functions of each coordination shell were taken from the lowest temperature (30 K) spectrum. The values of the first three cumulants C_i, relative to the low-temperature reference, were treated as free parameters, while the coordination numbers were constrained at the crystallographic values. For the first shell, an analysis based on the ratio method allowed to independently evaluate the significant influence of C_3 on the obtained C_1 values [61]. The relative values of cumulants $\Delta C_i^*(T)$ of the real distribution were calculated from C_i assuming $C_i^* = C_i$ for $i > 1$, and

$$C_1^* = C_1 + 2C_2[1/C_1 + 1/\lambda(k)], \tag{1}$$

with a photoelectron mean free path $\lambda = 10$ Å.

The first (0.7 to 2.0 Å), fourth (4.3 to 5.6 Å), and fifth (5.9 to 6.8 Å) peaks in FTs (see Fig. 4) are well isolated: thus their contributions could be easily singled out by Fourier back-transform. Since they are dominated by single-scattering processes (Re_0-O_1, Re_0-Re_4, and Re_0-Re_6, respectively), a standard single-scattering analysis was performed within the reduced k-space ranges 2–14, 5–14, and 7–14 Å^{-1}, respectively, to extract the cumulant values. Although the fourth and fifth peaks contain signals from both rhenium and oxygen scatterers, the oxygen contributions could be neglected at high k values, due to the large difference in the rhenium and oxygen backscattering amplitudes. Besides, according to the *ab initio* analysis, the lighter oxygen atoms in the outer shells have much larger second cumulants with respect to the heavier rhenium atoms, therefore their contribution to the EXAFS signal decreases so rapidly with increasing wave vector that only the rhenium contribution is significant at $k > 4$ Å^{-1}.

Also, the contribution from the second shell was singled out by Fourier back-transform within the range 2.9–4.1 Å and analyzed in the single-scattering approximation within the reduced k-space range 4–16 Å^{-1}. This approach to the analysis of the second shell, contaminated by MS contributions, is justified by the fact that the three signals (paths 3, 5, and 8 in Table I), according to the *ab initio* analysis, have similar values and temperature dependencies of the second cumulants.

The semiempirical data analysis was aimed at maximizing the amount of information directly available from experimental data for the first-, fourth-, and sixth-shell contributions. The inclusion of the third cumulant in the first-shell analysis increased the $\Delta C_1^*(600\ \mathrm{K})$ value of 1.5×10^{-3} Å, with a $\Delta C_3(600\ \mathrm{K})$ value of 5.5×10^{-5} Å. This difference is, in absolutes, a quite low value, but is significant in the present case, where the bond thermal expansion is extremely low (see Fig. 9). The statistical uncertainty of the fitting and cross-comparison procedures is represented by error bars in the figures, whenever larger than the data markers.

IV. RESULTS

It is convenient to divide the presentation of the results into three parts: thermal expansion measured by XRD, parallel MSRDs measured by EXAFS, and thermal expansion measured by EXAFS.

A. XRD results and lattice thermal expansion

The Bragg scattering from $\mathrm{ReO_3}$ crystal planes (100), (110), (210), (211), (222), (320), and (321) was recorded in the ESXD mode [47] in the temperature range from 300 to 603 K. Each diffraction peak was independently best-fitted to a Gaussian profile, and thus, its energy position was obtained. In the ESXD mode, the lattice spacings are related to the energy peak position as $d = ch/2E\,\sin(\theta)$, where 2θ is the fixed scattering angle of the detector. Finally, the lattice parameters $a_0(T)$ were calculated from the spacings d for each temperature. The accuracy of the Bragg peak position determination was $\Delta E/E \simeq 10^{-3}$, which corresponds to the accuracy in the lattice constant $\Delta a/a_0 \simeq 0.5 \times 10^{-4}$.

The temperature dependence of the lattice parameter calculated for the more intense Bragg-scattering peaks (100), (210), and (211) as well as their average curves are shown in Fig. 6. It is characterized by a weak variation, contained within 0.002 Å from 300 to 600 K. The thermal expansion is positive from 300 up to 470 K, decreases to 0 around 500 K and becomes negative from about 500 to 600 K.

The thermal expansion coefficient measured in the present work, $\alpha \simeq 2.6 \times 10^{-6}\ \mathrm{K^{-1}}$ from 300 to 470 K, is larger than that measured in previous works [12,21,35,36] but comparable to the expansion recently obtained [38] for the isostructural cubic $\mathrm{WO_3}$, $\alpha \simeq 3.9 \times 10^{-6}\ \mathrm{K^{-1}}$ between 300 and 500 K.

Since no internal coordinates are necessary to describe the structure of $\mathrm{ReO_3}$, the distances between atomic positions are directly proportional to the lattice constant, and their thermal expansions are proportional to the lattice thermal expansion. However, the lack of XRD data below 300 K, in principle, prevents the comparison with EXAFS data in order to evaluate the perpendicular MSRDs according to Eq. (2) in Sec. IV C. To overcome this difficulty, an independent evaluation of the lattice parameter thermal expansion, as well as its extrapolation below 300 K, has been attempted starting solely from the EXAFS data and is described below.

B. Parallel MSRDs

The second cumulants (parallel MSRDs) obtained from the *ab initio* and single-shell analyses of EXAFS spectra are shown in Figs. 7 and 8 for the Re-O and Re-Re distances, respectively. The *ab initio* approach gives *absolute* values of the MSRDs (open symbols), whose reliability depends on the accuracy of calculated scattering amplitudes and phase shifts. The semiempirical single-shell approach gives only MSRD values *relative* to the low-temperature reference spectrum; absolute values and the presence of a static contribution to MSRD can be evaluated by comparing the *ab-initio* results with the Einstein model [62], in particular at low temperatures. The error bars for the semiempirical values are smaller than the symbol width. Information on the third coordination shell ($\mathrm{O_3}$) could be obtained only by the *ab initio* approach. Conversely, the semiempirical approach allowed us to determine the parallel MSRD for the sixth coordination shell ($\mathrm{Re_6}$), which has a relatively low amplitude (peak at 6.3 Å in Fig. 4) and is hardly accessible to the *ab initio* analysis.

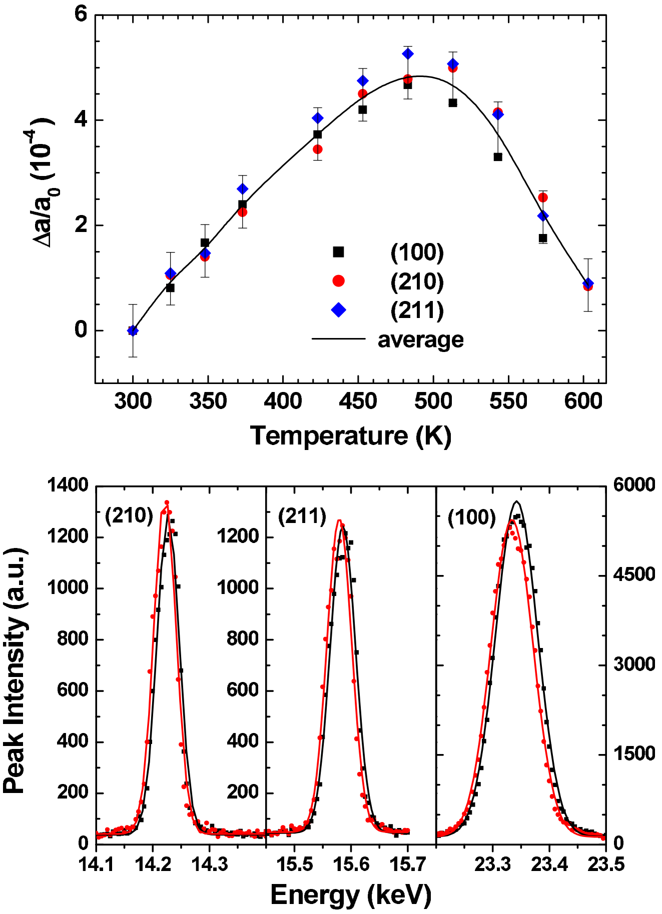

FIG. 6. (Color online) Top: Temperature dependence of the variation of the $\mathrm{ReO_3}$ lattice parameter $\Delta a(T)/a_0$, measured by ESXD in the temperature range from 300 to 603 K. Bottom: Example of the Bragg-scattering peaks from $\mathrm{ReO_3}$ crystal planes (100), (210), and (211) recorded at 300 K (black line) and 513 K [gray (red) line].

For the $\mathrm{Re_0}$-$\mathrm{O_1}$ distance, the absolute MSRD values from FEFFIT (open circles in Fig. 7) are lower than those from the Einstein model best fitting the temperature dependence of the semiempirical values (filled circles), while the agreement on temperature dependence is quite satisfactory. Since we cannot easily justify a constant reduction of the MSRD with respect to the Einsten model, we attribute this little

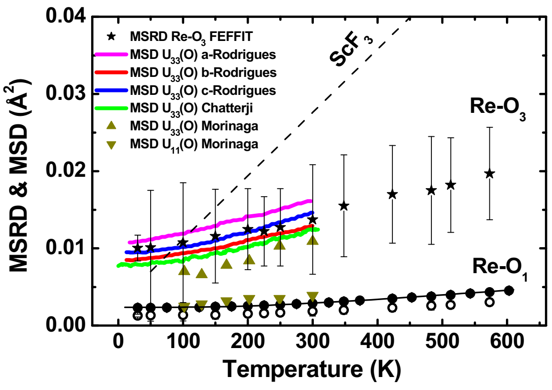

FIG. 7. (Color online) Temperature dependence of the second cumulants (parallel MSRDs) of the Re$_0$O$_1$ and Re$_0$-O$_3$ distances. Open and filled circles refer to results from FEFFIT and single-shell EDA analysis, respectively, for Re$_0$-O$_1$. Stars are the FEFFIT results for Re$_0$-O$_3$. Also shown are the uncorrelated anisotropic MSDs of O atoms perpendicular or parallel to the Re$_0$-O$_1$-Re$_2$ bond measured by Morinaga *et al.* [22] [(olive-green) triangles: upward, perpendicular; downward, parallel), by Chatterij *et al.* [32] (green line), and by Rodriguez *et al.* [33] (different powdered samples according to Ref. [33]: ReO$_3$-a, magenta line; ReO$_3$-b, red line; ReO$_3$-c, blue line). The dashed line represents the data for the parallel MSDs of fluorine in SrF$_3$ from Ref. [9].

discrepancy to residual inaccuracy of the *ab initio* calculations. These values are very similar in magnitude and in temperature dependence to the experimental values of the O$_1$ MSDs parallel to Re$_0$-O$_1$ bonds, measured by diffraction. For clarity, we present in Fig. 7 (downward olive-green triangles) only the data from Morinaga *at al.* [22].

For the Re$_0$-O$_3$ distance, absolute values of the parallel MSRD are obtained by the *ab initio* approach (stars in Fig. 7). These average absolute values are quite high in comparison with those evaluated by best-fitting their temperature dependence with an Einstein model. This may be attributed to the non-negligible contribution of static disorder, since the behavior of the purely thermal contribution to the MSRD is usually well approximated by the Einstein model. However, it is interesting to note that the temperature dependence of the parallel MSRD for Re$_0$-O$_3$ distances and of the experimental values of perpendicular MSDs of O$_1$ measured by diffraction are similar. According to the ReO$_3$ structure (see Fig. 1), considering the contribution of Re displacements and the correlation effects between Re$_0$ and O$_3$ atoms negligible, the thermal behaviors of the parallel MSRD for the Re$_0$-O$_3$ distance and of the uncorrelated amplitude of the O$_3$ MSD (MSD perpendicular to the Re$_2$-O$_3$-Re$_4$ chain, which is equivalent to the O$_1$ MSD perpendicular to the Re$_0$-O$_1$-Re$_2$ chain) should be comparable.

The parallel MSRDs for the Re$_0$-Re$_2$, Re$_0$-Re$_4$, and Re$_0$-Re$_6$ distances are shown in Fig. 8. The temperature dependencies from the semiempirical approach (filled symbols) are well fitted by Einstein models; the available absolute FEFFIT values can be considered in agreement with the semiempirical values, within the error bars. It is remarkable that the MSRD for the Re$_0$-Re$_4$ distance (face diagonal) is larger than the MSRD for the Re$_0$-Re$_6$ distance (cube diagonal), indicating a lower correlation for the fourth shell. A comparison of the EXAFS results with the low-temperature diffraction data is shown in the lower panel in Fig. 8, where we have plotted the values of twice the uncorrelated Re-Re MSDs from Morinaga *et al.* [22] (crosses) and from Chatterij *et al.* [32] (stars), as well as from Jørgensen *et al.* [18] (hexagons) at 300 K. It is evident that the EXAFS monitors a strong correlation of atomic motion only for the Re$_0$-Re$_2$ distance, while a comparison with the data from Chatterij *et al.* indicates a negligible correlation for the fourth-shell distance.

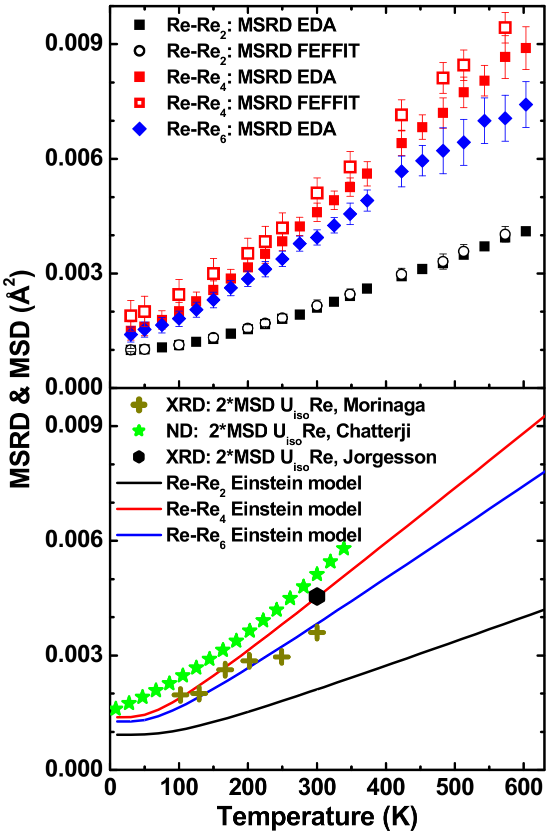

FIG. 8. (Color online) Top: Temperature dependence of the second cumulants (parallel MSRDs) of the Re$_0$-Re$_2$ (black circles), Re$_0$-Re$_4$ [(red) squares], and Re$_0$-Re$_6$ [(blue) diamonds] distances. Open and filled symbols refer to results from FEFFIT and EDA analysis, respectively. Bottom: Einstein model of parallel MSRDs best fitting the presented data from EXAFS cumulant analysis (lines) and uncorrelated MSDs of Re atoms measured by Morinaga *et al.* [22] (crosses), Jørgensen *et al.* [18] (hexagons), and Chatterij *et al.* [32] (stars).

The parallel MSRDs obtained in this work are in agreement, within the error bars, with our previous results [29,30] for the Re$_0$-O$_1$ distance at low temperatures ($T < 350$ K) and for the Re$_0$-Re$_4$ distance over the whole interval of temperatures. The main difference occurs for the Re$_0$-O$_1$ MSRD at high temperatures ($T > 350$ K) and is attributed to the fact that the previous experiments were performed in air.

C. First cumulants and bond thermal expansions

The normalized relative values $\Delta C_1^*/C_1^*(30\,\mathrm{K})$ [where $\Delta C_1^* = C_1^*(T) - C_1^*(30\,\mathrm{K})$] of the first cumulants for the Re$_0$-O$_1$ (nearest-neighbor) and Re$_0$-Re$_4$ (face-diagonal)

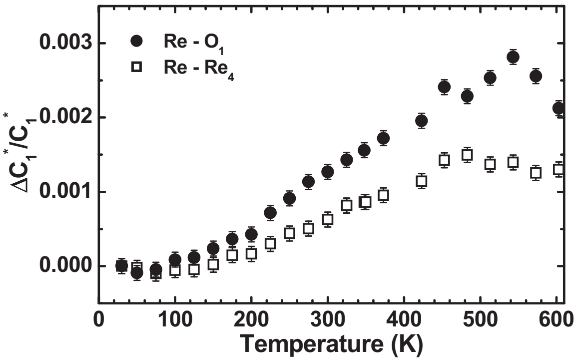

FIG. 9. Normalized relative temperature dependence of the first cumulants for the first-shell Re_0-O_1 distance (circles) and the fourth-shell Re_0-Re_4 distance (squares), extracted by single-shell analysis.

distances, obtained by the semiempirical method, are shown in Fig. 9. A comparison with our previous studies of ReO_3 indicates that the first cumulant accuracy in this work is two orders of magnitude better [29].

Both Re_0-O_1 and Re_0-Re_4 distances share the same *s*-shaped behavior: weak negative expansion below 100 K, positive expansion from 150 to 450 K, and negative expansion above 500 K. The larger bond thermal expansion shown by the first shell is attributable to the larger perpendicular displacements of O_1 atoms with respect to Re_4 atoms. We may remember, anyway, that in many other cases EXAFS monitored a larger bond thermal expansion of the first-shell distance: this is, in general, interpreted in terms of a smaller vibrational anisotropy in the outer shells, as confirmed by experimental and theoretical studies [61,63].

The difference between the average bond distances $\langle r \rangle = C_1^*$ measured by EXAFS and the distance between average atomic positions R measured by Bragg diffraction is due to the perpendicular MSRD $C_\perp = \langle \Delta u_\perp^2 \rangle$ [42,43]:

$$\langle r \rangle = R + \langle \Delta u_\perp^2 \rangle / 2R \,. \tag{2}$$

Usually, from Eq. (2) the perpendicular MSRD is derived, thus providing relevant insights on the relation between local dynamical behavior and macroscopic NTE [40,45]. In the present case of ReO_3, however, while the bond thermal expansion ΔC_1^* could be measured by EXAFS for the first and fourth shells over the full temperature range from 30 to 600 K, the lattice thermal expansion could be measured by diffraction only above 300 K.

We have tried to evaluate also below 300 K the lattice thermal expansion Δa (corresponding to the distance between average Re atomic positions along the main cubic axes) on the basis of fourth-shell data, for which we have already shown that the correlation for the Re_0-Re_4 distance is negligible. The relation between the projections, parallel and perpendicular to a given direction, of both MSDs and MSRDs depends on the peculiar dynamical properties of a given crystal. Since the MSD of rhenium atoms is isotropic, we have considered reasonable the assumption that the MSRD for the Re_0-Re_4 distance is also isotropic, $\langle \Delta u_\perp^2 \rangle = 2 \langle \Delta u_\parallel^2 \rangle$, and evaluated its perpendicular MSRD from the measured parallel MSRD.

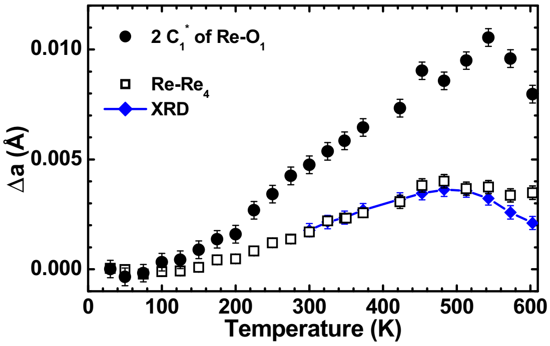

FIG. 10. (Color online) Variation with temperature of the ReO_3 lattice parameter, measured by ESXD above 300 K [filled (blue) diamonds] and calculated from the EXAFS first cumulant of the fourth shell (open black squares). Filled black circles represent twice the variation of the EXAFS first cumulant of the first shell.

Once the perpendicular MSRD for the fourth-shell Re_0-Re_4 distance was determined, it was possible to evaluate the corresponding crystallographic expansions by inverting Eq. (2) and, by proportionality, to calculate the variation with temperature of the lattice thermal parameter Δa (see Fig. 10; open black squares). The agreement with the XRD data above 300 K [see Fig. 10; filled (blue) diamonds] is good, and supports the extrapolation of the lattice thermal expansion below 300 K, based on EXAFS data for the 4th shell.

Let us now consider again the first coordination shell. In the undistorted perovskite structure (see Fig. 1), the lattice parameter a_0 is exactly twice the Re_0-O_1 distance. In Fig. 10, the first-shell thermal expansion multiplied by 2, $2\Delta C_1^*$ (filled black circles), is compared with the lattice thermal expansion Δa [filled (blue) diamonds and open black squares]. According to Eq. (2), the difference is due to the growth with temperature of the first-shell perpendicular MSRD $C_\perp = \langle \Delta u_\perp^2 \rangle$.

This is the last result of our analysis: it is now possible to compare the temperature variations of both parallel and perpendicular MSRDs relative to the first Re_0-O_1 shell, together with those of uncorrelated MSDs of O atoms. Their relative values are shown in Fig. 11.

Our choice to compare 1/2 $\Delta C_\perp(T)$ values with $\Delta C_{||}(T)$ allows us to evaluate the difference between parallel and perpendicular vibrations. This difference is an expected result, since the absolute displacement ellipsoids of oxygen atoms measured by diffraction are strongly anisotropic (see, for example, the upward and downward triangles in Fig. 7). However, the temperature dependence of the variation of the first-shell perpendicular 1/2 MSRD is much weaker than the variation of uncorrelated MSDs of O atoms measured by diffraction (see Fig. 11) as well as of the third-shell (Re_0-O_3) parallel MSRD (see Fig. 7). An explanation of this apparent discrepancy is given in the following Discussion.

V. DISCUSSION

The experimental results obtained in the present work from the complex analysis of XRD and EXAFS data measured contemporaneously are now discussed and compared with recently published experimental and theoretical work by different authors.

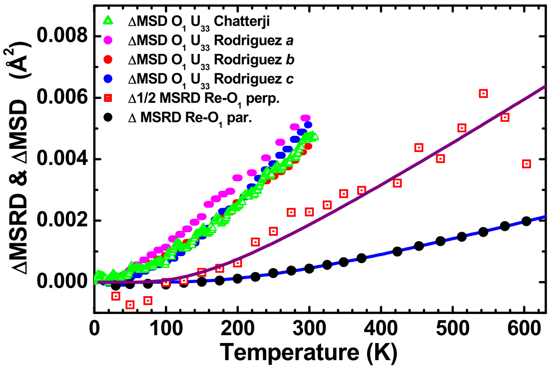

FIG. 11. (Color online) Temperature dependence of MSRDs (parallel) and 1/2 MSRDs (perpendicular) for the Re_0-O_1 distance (filled black circles) and [open (red) squares] for parallel and perpendicular projections, respectively. Also shown is the variation of uncorrelated MSDs of oxygen atoms (ΔMSD perpendicular to the Re_0-O_1-Re_2 bond), measured by Chatterij *et al.* [32] [(green) triangles] and Rodriguez *et al.* [33] (different powdered samples according to Ref. [33]: ReO_3-a, magenta circles; ReO_3-b, red circles; and ReO_3-c, blue circles).

A. On experimental results from different experiments

The present XRD and EXAFS results agree well with all those published up to now: ReO_3 is characterized by a very weak thermal expansion. Small quantitative differences do not influence the main comparison with other NTE materials, and should be analyzed with care, because their origin is not univocally understood. The lattice thermal expansion of ReO_3 measured in this work has an *s*-shaped behavior characterized by a weak negative expansion below about 100 K, a weak positive expansion (about 2.6×10^{-6} K^{-1}) from 150 to 500 K, and, again, a negative expansion above 500 K.

The present behavior of thermal expansion is in qualitative agreement with the most recent neutron and x-ray diffraction studies [11,31–33]: it is shown in Fig. 2 that the transition from negative to positive thermal expansion depends significantly on the sample; moreover, both our data and recent neutron data evidence a second negative trend at high temperatures (above 500–600 K).

A quantitative comparison of thermal expansion behavior and MSD data indicates that the differences between the many published experiments depend on samples, but at present it is impossible to define why and how. The differences among the three samples carefully measured in Ref. [33] were attributed to the "original sample quality." In our opinion many parameters should be taken into consideration; for example, the grinding process or even the manipulation of powders in air when mounting on sample holders for XRD and EXAFS experiments was sufficient, in our experience, to produce slightly different EXAFS signals and thermal trends. The comparison of experiments from different groups and techniques is at present an open problem. At any rate, if we consider the absolute changes in the thermal expansion coefficient measured for ReO_3 in comparison with the general trend of ScF_3, it is evident that these effects are not able to produce significant modifications from the average behavior of ReO_3.

Further consideration can be given to the different MSD values measured by x-ray or neutron diffraction studies, in comparison with some expected values estimated from calculations [64]: while at least a qualitative agreement was found between models and experimental values for U_{iso}(Re) and U_{11}(O) (but with increasing deviation at increasing temperature), U_{33}(O) (component perpendicular to Re-O-Re chains) remained highly underestimated. The measured MS vibrations were much higher with respect to the calculated vibrations, and the authors suggested that the observed mismatch is predominantly due to a static component which is not taken into account in *ab initio* calculations. This static component, however, is different for each sample, as clearly shown in Figs. 7 and 8.

Recent Raman studies of ReO_3 are also consistent with the presence of static disorder, which lowers the local symmetry. A locally undistorted ReO_3 crystal should have no Raman active modes, because of its cubic symmetry; however, appreciable Raman signals were recently detected by Purans *et al.* [65]. This result was explained in terms of disorder-induced scattering by the bulk structure of cubic ReO_3.

B. Geometrical models

The behavior of ReO_3 below 500 K (i.e., negative expansion up to 100 K and positive expansion between 150 and 500 K) is shared by many NTE materials with a diamond-zincblende structure, where the total expansion originates from an interplay of a positive contribution due to a bond-stretching effect, caused by the asymmetry of the pair potential, and a negative contribution due to a tension effect, caused by a component of the relative atomic motion being transverse to the bond direction [1]. Vibrational modes giving rise to the tension effect prevail at low temperatures over modes giving rise to the stretching effect.

In framework structures, the possibility of relative rotations of tetrahedral and/or octahedral structural units can give rise to low-frequency RUMs, which induce NTE extending over large temperature intervals [3,7,8]. The peculiar structure of ReO_3, made up by corner-sharing ReO_6 octahedra, seems particularly suitable for supporting RUMs. Actually, Tao and Sleight [5] have shown that RUM motions exist in ReO_3 for all wave vectors $\{1/2,1/2,\zeta\}$, corresponding to "rocking motions" of octahedra along each of the three axes. Besides, the structure of ReO_3, when projected on the x-y plane (see Fig. 12), corresponds to the simplest two-dimensional framework structure that is commonly used to explain the connection between RUMs and NTE. From Fig. 12(a), we can derive the effects on the distances measured by EXAFS of a simple static deformation produced by the rotation of ReO_6 octahedra: the second-shell Re-Re_2 is shortened, and the third-shell Re-O_3 is split into two slightly different distances. The latter effect produces a static contribution to the Debye-Waller factor in the EXAFS analysis of the peak. In addition, according to the RUM model, small continuous rotations around one or more of the main axes will also produce a shortening of the apparent bond Re-O_1 and an increase in the MSD measured by XRD, in particular, in the direction perpendicular to the Re-O-Re chains. However, we have seen that some of the measured MSDs are quite high even at low

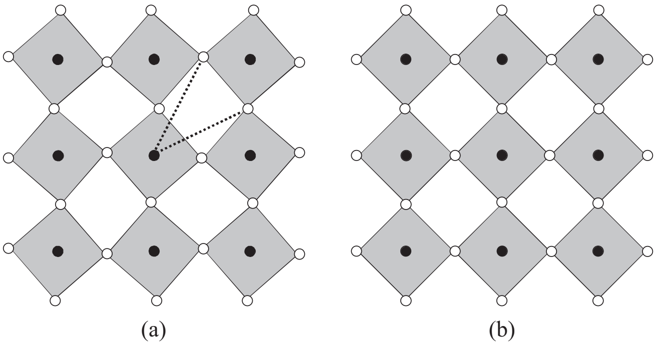

FIG. 12. Two-dimensional model of a perovskite-like structure: filled and open circles represent rhenium and oxygen atoms, respectively. Left: Distorted equilibrium configuration, with $\langle\theta\rangle = 4^\circ$; dashed lines represent the two Re_0-O_3 distances. Right: Undistorted configuration.

temperatures, and this can only be explained by a certain degree of static disorder.

A geometric model based on experimental evidence should thus start from the presence of a significant static disorder already at low temperatures, as measured by EXAFS and diffraction, but with the exclusion of large rotations and of long-range deformation with respect to a cubic structure, as documented in recent studies by total neutron scattering, including Rietveld and accurate PDF analysis [34].

We propose a model able to qualitatively explain why ReO_3, in spite of the possibility of supporting RUMs, shows a small but positive expansion from about 100 K up to at least 500 K and the presence of a second NTE range at higher temperatures. The explanation is based on the hypothesis that RUMs correspond to librations of the octahedra with respect to a rotated, but disordered configuration, where the Re-O-Re linkage angle is not 180° (see Fig. 12, left). A similar picture was proposed in Ref. [24] to explain the local behavior of antiferrodistortive phase transitions in some perovskite structures and was also considered for ReO_3 in Ref. [23].

The different effects of RUMs with respect to undistorted and to distorted equilibrium configurations [4] have been discussed in Ref. [1] with reference to a two-dimensional model and are here shortly resumed. If RUMs induce rotations around an undistorted equilibrium configuration (see Fig. 12, right), the apparent bond length R is connected to the true bond length $\langle r\rangle$ by the relation

$$R = \langle r\rangle[1 - \langle\theta^2\rangle/2], \tag{3}$$

where θ is the rotation angle, and $\langle\theta\rangle = 0$. When the temperature increases, $\langle\theta^2\rangle$ increases, and RUMs induce NTE.

Let us now consider an equilibrium distorted configuration, characterized by $\langle\theta\rangle \neq 0$ (see Fig. 12, left), and let this distortion decrease ($\langle\theta\rangle \to 0$) when the temperature increases. The instantaneous rotation can be expressed as $\theta = \langle\theta\rangle + \epsilon$, and the relation between apparent and true bond lengths becomes [1]

$$R = \langle r\rangle \cos\langle\theta\rangle[1 - \langle\epsilon^2\rangle/2] \,. \tag{4}$$

The factor $\cos\langle\theta\rangle$ increases with temperature, because $\langle\theta\rangle$ decreases towards 0 and gives rise to a positive contribution to lattice expansion. The last factor $[1 - \langle\epsilon^2\rangle/2]$ corresponds to the usual negative contribution of RUMs to thermal expansion. The total lattice expansion results from the positive contributions of $\langle r\rangle$ and $\cos\langle\theta\rangle$ and from the negative contribution of $[1 - \langle\epsilon^2\rangle/2]$. When $\langle\theta\rangle$ reaches the undistorted equilibrium configuration $\langle\theta\rangle = 0$, the positive contribution $\cos\langle\theta\rangle$ disappears, and NTE develops again.

In a three-dimensional space, the model describes the structure of ReO_3 below 500 K as a locally distorted perovskite structure, where the octahedra may be slightly rotated by an angle $\langle\theta\rangle$ (static disorder). This leads to a local distortion where symmetry is lower than ($Pm\bar{3}m$) and to different Re-O_3 distances. The small deviation is, however, only a local property, randomly distributed in terms of space and orientation, and only contributes to the MSD in diffraction experiments. When the average angle $\langle\theta\rangle$ becomes 0, the equilibrium situation corresponds to the regular perovskite structure, and the negative contribution due to RUMs is no longer counterbalanced by the decrease in $\langle\theta\rangle$, thus explaining the onset of NTE at about 500 K.

Consistent with this picture is the weaker temperature dependence found for the Re_0-O_1 perpendicular MSRD with respect to the uncorrelated MSDs of oxygen atoms (see Fig. 11). Actually, the reduction in $\langle\theta\rangle$ when the temperature increase below 500 K corresponds to a negative contribution to the increase in $\langle\Delta u_\perp^2\rangle$.

Very recently this geometrical approach has been used to explain the almost-zero thermal expansion of a TaO_2F, where off-axis displacements of oxygen and fluorine atoms were observed, and the strong positive thermal expansion of rhombohedrally distorted AlF_3, until this crystallographic bond angle approaches 180° [66].

C. Final considerations

The geometrical approach is simple and intuitive but often criticized for its lack of a quantitative description of detailed and different experimental observations. At times, the search for the basic “rigid unit” to be considered in modeling NTE has been critically questioned by people used to working within the lattice dynamics approach. Two very recent contributions [67,68] (both with M. T. Dove as coauthor) tried to fill this gap, with results of interest for the present discussion on ReO_3.

The first contribution contains a generalized model able to describe rigid and flexible relations of atoms along a chain where transverse motions are allowed, but bond lengths are constrained [67]. It is clearly shown that, by a convenient balance of force constants and anharmonic terms, the general behavior of NTE materials can be described and controlled. The model allows us also to see how the relative importance of low-frequency modes, which are mainly responsible for NTE, is changed at increasing temperatures.

The second contribution follows the reverse route: it starts from high-quality *ab initio* calculations of lattice dynamics (of Cu_2O) and compares the obtained phonon dispersion curves with vibrational models containing some predefined constrains on bond rigidity and framework flexibility [68]. According to the authors, the main contribution to NTE, in the investigated case, comes from acoustic vibrations of rigid O-Cu-O rods. This confirms the presence of RUM modes but results in a partial contradiction to the previous hypothesis, because the expected influence of OCu_4 tetrahedra and of Cu-O rods is evaluated to be of minor importance from the calculations.

Returning to ReO_3, we can easily recognize, in addition to the ReO_6 octahedra, the presence of -O-Re-O- or -Re-O-Re- chains whose dynamics could be studied in a way similar to that in Refs. [67] and [68]. The small (but significant) experimental differences in the measured thermal expansion (see Fig. 2) do not allow an unequivocal quantitative comparison: the presence of local defects or distortions is probably sufficient to modify the local dynamics or to introduce nonharmonic terms, thus justifying the different observed (and apparently contradictory) behaviors. The analysis in terms of chains and of transverse motion is interesting also if we consider the Re-O_1-Re_2 units. EXAFS detects a high correlation of Re-Re_2 movements parallel to the chains, much stronger than that of the diagonal distances Re-Re_4 and Re-Re_6. On the other hand, diffraction measurements found almost-comparable MSD values for U_{iso}(Re) and U_{11}(O). This means that the Re-O_1-Re_2 basic units can move almost rigidly in longitudinal directions, while transverse vibrations involving the Re-Re edges of the main cubic structure can locally distort the structure. Since low-frequency modes involving Re atoms are the main components of the phonon density of states below 5 THz [64], they probably contribute to the NTE of ReO_3, just in the low-temperature range where all experiments found a small negative expansion.

VI. CONCLUSIONS

Temperature-dependent EXAFS measurements provide original information on the local atomic structure and dynamics of materials with framework oxide structures, which exhibit negative or ultralow thermal expansion. In this work, we have presented the results of a joint EXAFS and XRD study of polycrystalline ReO_3 over the whole temperature range of stability of the cubic structure at ambient pressure.

We have presented a detailed EXAFS analysis of ReO_3 up to the sixth coordination shell. According to our results, ReO_3 exhibits ultralow thermal expansion over the whole temperature range explored: negative thermal expansion below 100 K, positive from 150 to 500 K, and negative again above 500 K.

The EXAFS results suggest the presence of some disordered rotations of the ReO_6 octahedra at ambient pressure, so that locally the Re-O-Re linkage is slightly rotated by an average angle $\langle\theta\rangle$ (lowering the local symmetry). This phenomenon could explain why ReO_3, in spite of the possibility of supporting RUMs over a wide temperature range as seen at low temperatures, has a positive expansion from about 150 K up to at least 500 K. NTE behavior is restored at higher temperatures, when $\langle\theta\rangle$ reaches a 0 value, and the tension effect activated by high-frequency rotations of ReO_6 prevails.

In the low-temperature range, EXAFS and XRD analyses support the idea that also correlated movements of Re atoms in the transverse direction with respect to the -Re-O-Re- chains should be taken into account to explain the NTE behavior in terms of RUMs.

ACKNOWLEDGMENTS

The authors acknowledge the support of the European Synchrotron Radiation Facility (ESRF Project HS2270). They are grateful to S. De Panfilis and the technical staff of the ESRF BM29 beam line for assistance during the experiments and to M. Dapiaggi for helpful discussions. This work was partially supported by Latvian Science Council Grant No. 402/2012. A.K. is grateful to the IFN-CNR (Trento) and Fondazione Bruno Kessler for hospitality and support.

---

[1] G. D. Barrera, J. A. Bruno, T. H. K. Barron, and N. L. Allan, J. Phys.: Condens. Matter **17**, R217 (2005).
[2] A. L. Goodwin, Z. Kristallogr. Suppl. **30**, 1 (2009).
[3] T. A. Mary, J. S. O. Evans, T. Vogt, and A. W. Sleight, Science **272**, 90 (1996).
[4] A. W. Sleight, Curr. Opin. Solid State Mater. Sci. **3**, 128 (1998).
[5] J. Tao and A. Sleight, J. Solid State Chem. **173**, 442 (2003).
[6] R. Mittal, M. Zbiri, H. Schober, E. Marelli, S. J. Hibble, A. M. Chippindale, and S. L. Chaplot, Phys. Rev. B **83**, 024301 (2011).
[7] A. K. A. Pryde, K. D. Hammonds, M. T. Dove, V. Heine, J. D. Gale, and M. C. Warren, J. Phys.: Condens. Matter **8**, 10973 (1996).
[8] V. Heine, P. R. L. Welche, and M. T. Dove, J. Am. Ceram. Soc. **82**, 1793 (1999).
[9] B. K. Greve, K. L. Martin, P. L. Lee, P. J. Chupas, K. W. Chapman, and A. P. Wilkinson, J. Am. Chem. Soc. **132**, 15496 (2010).
[10] J. Purans, G. Dalba, P. Fornasini, A. Kuzmin, S. D. Panfilis, and F. Rocca, AIP Conf. Proc. **882**, 422 (2007).
[11] M. Dapiaggi and A. N. Fitch, J. Appl. Crystallogr. **42**, 253 (2009).
[12] T. S. Chang and P. Trucano, J. Appl. Crystallogr. **11**, 286 (1978).
[13] A. Fujimori and N. Tsuda, Solid State Commun. **34**, 433 (1980).
[14] P. B. Allen and W. W. Schulz, Phys. Rev. B **47**, 14434 (1993).
[15] C. N. King, H. C. Kirsch, and T. H. Geballe, Solid State Commun. **9**, 907 (1971).
[16] T. P. Pearsall and C. A. Lee, Phys. Rev. B **10**, 2190 (1974).
[17] T. Tanaka, T. Akahane, E. Bannai, S. Kawai, N. Tsuda, and Y. Ishizawa, J. Phys. C: Solid State Phys. **9**, 1235 (1976).
[18] J. E. Jørgensen, J. D. Jørgensen, B. Batlogg, J. P. Remeika, and J. D. Axe, Phys. Rev. B **33**, 4793 (1986).
[19] F. S. Razavi, Z. Altounian, and W. R. Datars, Solid State Commun. **28**, 217 (1978).
[20] B. Batlogg, R. G. Maines, M. Greenblatt, and S. Di Gregorio, Phys. Rev. B **29**, 3762 (1984).
[21] J. E. Schirber and B. Morosin, Phys. Rev. Lett. **42**, 1485 (1979).
[22] M. Morinaga, K. Sato, J. Harada, H. Adachi, S. Ohba, and Y. Saito, J. Phys. C: Solid State Phys. **16**, L177 (1983).
[23] B. Houser and R. Ingalls, Phys. Rev. B **61**, 6515 (2000).
[24] B. Rechav, Y. Yacoby, E. A. Stern, J. J. Rehr, and M. Newville, Phys. Rev. Lett. **72**, 1352 (1994).

[25] A. Kalinko, R. Evarestov, A. Kuzmin, and J. Purans, J. Phys.: Conf. Ser. **190**, 012080 (2009).

[26] J. Timoshenko, A. Kuzmin, and J. Purans, Comput. Phys. Commun. **183**, 1237 (2012).

[27] N. Alberding, E. D. Crozier, R. Ingalls, and B. Houser, J. Phys. (Paris) **47**, 681 (1986).

[28] A. Kuzmin, J. Purans, M. Benfatto, and C. R. Natoli, Phys. Rev. B **47**, 2480 (1993).

[29] G. Dalba, P. Fornasini, A. Kuzmin, J. Purans, and F. Rocca, J. Phys.: Condens. Matter **7**, 1199 (1995).

[30] A. Kuzmin, J. Purans, G. Dalba, P. Fornasini, and F. Rocca, J. Phys.: Condens. Matter **8**, 9083 (1996).

[31] T. Chatterji, P. F. Henry, R. Mittal, and S. L. Chaplot, Phys. Rev. B **78**, 134105 (2008).

[32] T. Chatterji, T. C. Hansen, M. Brunelli, and P. F. Henry, Appl. Phys. Lett. **94**, 241902 (2009).

[33] E. E. Rodriguez, A. Llobet, T. Proffen, B. C. Melot, R. Seshadri, P. B. Littlewood, and A. K. Cheetham, J. Appl. Phys. **105**, 114901 (2009).

[34] E. S. Božin, T. Chatterji, and S. J. L. Billinge, Phys. Rev. B **86**, 094110 (2012).

[35] N. Matsuno, M. Yoshimi, S. Ohtake, T. Akahane, and N. Tsuda, J. Phys. Soc. Jpn. **45**, 1542 (1978).

[36] N. Tsuda, Y. Sumino, I. Ohno, and T. Akahane, J. Phys. Soc. Jpn. **41**, 1153 (1976).

[37] D. Taylor, Br. Ceram. Trans. J. **84**, 9 (1985).

[38] W. Crichton, P. Bouvier, and A. Grzechnik, Mater. Res. Bull. **38**, 289 (2003).

[39] G. Dalba, P. Fornasini, R. Grisenti, and J. Purans, Phys. Rev. Lett. **82**, 4240 (1999).

[40] A. Sanson, F. Rocca, G. Dalba, P. Fornasini, R. Grisenti, M. Dapiaggi, and G. Artioli, Phys. Rev. B **73**, 214305 (2006).

[41] G. Beni and P. M. Platzman, Phys. Rev. B **14**, 1514 (1976).

[42] W. R. Busing and H. A. Levy, Acta Crystallogr. **17**, 142 (1964).

[43] P. Fornasini, J. Phys.: Condens. Matter **13**, 7859 (2001).

[44] S. a Beccara, G. Dalba, P. Fornasini, R. Grisenti, A. Sanson, and F. Rocca, Phys. Rev. Lett. **89**, 025503 (2002).

[45] M. Vaccari, R. Grisenti, P. Fornasini, F. Rocca, and A. Sanson, Phys. Rev. B **75**, 184307 (2007).

[46] A. Filipponi, M. Borowski, D. T. Bowron, S. Ansell, S. De Panfilis, A. Di Cicco, and J. P. Itié, Rev. Sci. Instrum. **71**, 2422 (2000).

[47] A. Filipponi, V. M. Giordano, S. De Panfilis, A. Di Cicco, E. Principi, M. Borowski, and J. P. Itié, Rev. Sci. Instrum. **74**, 2654 (2003).

[48] N. A. el All, B. T. Sendja, R. Grisenti, F. Rocca, D. Diop, O. Mathon, S. Pascarelli, and P. Fornasini, J. Synchrotron Radiat. **20**, 603 (2013).

[49] A. Kuzmin, Physica B **208–209**, 175 (1995).

[50] D. R. Lide (ed.), *CRC Handbook of Chemistry and Physics* (CRC Press, Boca Raton, FL, 1990).

[51] A. Kuzmin and J. Purans, J. Phys.: Condens. Matter **5**, 267 (1993).

[52] A. Ankudinov, B. Ravel, J. Rehr, and S. Conradson, Phys. Rev. B **58**, 7565 (1998).

[53] J. Rehr and R. Albers, Rev. Mod. Phys. **72**, 621 (2000).

[54] M. Newville, J. Synchrotron Radiat. **8**, 322 (2001).

[55] J. J. Rehr, J. M. de Leon, S. I. Zabinsky, and R. C. Albers, J. Am. Chem. Soc. **113**, 5135 (1991).

[56] J. M. de Leon, J. J. Rehr, S. I. Zabinsky, and R. C. Albers, Phys. Rev. B **44**, 4146 (1991).

[57] E. A. Stern, D. E. Sayers, and F. W. Lytle, Phys. Rev. B **11**, 4836 (1975).

[58] M. Vaccari and P. Fornasini, Phys. Rev. B **72**, 092301 (2005).

[59] G. Bunker, Nucl. Instrum. Methods Phys. Res. **207**, 437 (1983).

[60] P. Fornasini, F. Monti, and A. Sanson, J. Synchrotron Radiat. **8**, 1214 (2001).

[61] P. Fornasini and R. Grisenti, J. Chem. Phys. **141**, 164503 (2014).

[62] M. Vaccari and P. Fornasini, J. Synchrotron Radiat. **13**, 321 (2006).

[63] S. Ahmed, G. Aquilanti, N. Novello, L. Olivi, R. Grisenti, and P. Fornasini, J. Chem. Phys. **139**, 164512 (2013).

[64] U. D. Wdowik, K. Parlinski, T. Chatterji, S. Rols, and H. Schober, Phys. Rev. B **82**, 104301 (2010).

[65] J. Purans, A. Kuzmin, E. Cazzanelli, and G. Mariotto, J. Phys.: Condens. Matter **19**, 226206 (2007).

[66] C. Morelock, B. Greve, M. Cetinkol, K. Chapman, and P. C. A. Wilkinson, Chem. Mater. **25**, 1900 (2013).

[67] H. Fang, M. T. Dove, and A. E. Phillips, Phys. Rev. B **89**, 214103 (2014).

[68] L. H. N. Rimmer, M. T. Dove, B. Winkler, D. J. Wilson, K. Refson, and A. L. Goodwin, Phys. Rev. B **89**, 214115 (2014).